

Photoproduction of neutral kaons on a liquid deuterium target in the threshold region

K. Tsukada, T. Takahashi,^{*} T. Watanabe,[†] Y. Fujii, K. Futatsukawa, O. Hashimoto, K. Hirose, K. Ito, S. Kameoka, H. Kanda, K. Maeda, A. Matsumura, Y. Miura, H. Miyase, S. N. Nakamura, H. Nomura, K. Nonaka, T. Osaka, Y. Okayasu, H. Tamura, H. Tsubota, M. Ukai,[†] H. Yamauchi, and M. Wakamatsu

Department of Physics, Tohoku University, Sendai 980-8578, Japan

T. Ishikawa, T. Kinoshita, F. Miyahara, T. Nakabayashi, H. Shimizu, T. Tamae, and H. Yamazaki

Laboratory of Nuclear Science, Tohoku University, Sendai 982-0826, Japan

A. Sasaki

Department of Electrical and Electronic Engineering, Akita University, Akita 010-8502, Japan

O. Konno

Department of Electrical Engineering, Ichinoseki National College of Technology, Ichinoseki 021-8511, Japan

P. Bydžovský and M. Sotona

Nuclear Physics Institute, 25068, Řež, Czech Republic

(Received 3 December 2007; published 9 July 2008)

The photoproduction process of neutral kaons on a liquid deuterium target is investigated near the threshold region, $E_\gamma = 0.8\text{--}1.1$ GeV. K^0 events are reconstructed from positive and negative pions, and differential cross sections are derived. Experimental momentum spectra are compared with those calculated in the spectator model using a realistic deuteron wave function. Elementary amplitudes as given by recent isobar models and a simple phenomenological model are used to study the effect of the new data on the angular behavior of the elementary cross section. The data favor a backward-peaked angular distribution of the elementary $n(\gamma, K^0)\Lambda$ process, which provides additional constraints on current models of kaon photoproduction. The present study demonstrates that the $n(\gamma, K^0)\Lambda$ reaction can provide key information on the mechanism of the photoproduction of strangeness.

DOI: [10.1103/PhysRevC.78.014001](https://doi.org/10.1103/PhysRevC.78.014001)

PACS number(s): 13.60.Le, 25.20.Lj

I. INTRODUCTION

Kaon production on a nucleon or a nucleus by the electromagnetic interaction provides invaluable information on the strangeness production mechanism, because the electromagnetic interaction is better understood than the hadronic interaction. Studies using real photon and electron beams were started in the early 1950s. The $p(\gamma, K^+)\Lambda$ reaction was studied from the threshold up to 1.4 GeV by measuring the differential cross sections [1–6], total cross sections [7], and Λ polarizations [3,5]. An experiment using the polarized target was also made [8]. The isobar model for kaon photoproduction was developed to reproduce the experimental results in the 1960s [9].

Since the 1990s, new experiments have been carried out using advanced detector systems at accelerator facilities that provide higher quality photon or electron beams. There are six isospin channels of elementary kaon photoproduction, $p(\gamma, K^+)\Lambda$, $p(\gamma, K^+)\Sigma^0$, $p(\gamma, K^0)\Sigma^+$, $n(\gamma, K^0)\Lambda$, $n(\gamma, K^0)\Sigma^0$, and $n(\gamma, K^+)\Sigma^-$, though kaon production reactions with proton targets have mainly been investigated to date.

The $p(\gamma, K^+)\Lambda$ reaction has been studied from the threshold region up to a photon energy of 2.95 GeV by measuring the differential and total cross sections at ELSA/SAPHIR [10], JLab/CLAS [11], and SPring-8/LEPS [12]. Polarization transfer in the $p(\vec{\gamma}, K^+)\bar{\Lambda}$ reaction has been also measured at CLAS [13], and the beam polarization asymmetries for the $p(\vec{\gamma}, K^+)\Lambda$ and $p(\vec{\gamma}, K^+)\Sigma^0$ reactions have been measured at SPring-8/LEPS [12]. To date, several theoretical models have been proposed [14–20]. Although a wide variety of observables in elementary kaon photoproduction processes has been investigated, no model has successfully explained them all. Therefore, further experimental and theoretical studies are eagerly awaited, particularly in other isospin channels. In particular, the $n(\gamma, K^0)\Lambda$ reaction is expected to greatly help clarify the strangeness photoproduction process. This reaction has the following features.

- (i) The Born term in the t channel does not contribute, in contrast to reactions with K^+ in the final state, because no charge is involved in the reaction.
- (ii) The strong coupling constants in the u channel for Σ^0 and other isovector exchanges have the same value but are of opposite sign to those in the $p(\gamma, K^+)\Lambda$ reaction because of the isospin symmetry.
- (iii) The electromagnetic coupling constants of resonances in the s and t channels, e.g., $g_{N^*n\gamma}$ and $g_{K^*K^0\gamma}$, are different than those in the K^+ photoproduction process.

^{*}Present address: Institute of Particle, Nuclear Studies, High Energy Accelerator Organization (KEK), Tsukuba, 305-0801, Japan.

[†]Present address: Gifu University, Gifu, 501-1193, Japan.

Because of these characteristics, the interference among the diagrams in the $K^0\Lambda$ production process is quite different from that in the $K^+\Lambda$ process. Because of this difference, it was indicated that the angular distribution of the $K^0\Lambda$ production process shows a backward peak [21]. Therefore, comparison of K^0 and K^+ photoproduction data, especially the angular distribution, is very important for the investigation of the strangeness photoproduction mechanism. Note that the absence of electric charge in the $K^0\Lambda$ process (the s -channel Born term is gauge invariant by itself) makes implementation of hadronic form factors easier than in the $K^+\Lambda$ case. In addition to the features mentioned above, the influence of the higher mass resonances can be considered to be small in the present experiment, which was carried out near the threshold, $E_\gamma = 0.8\text{--}1.1$ GeV.

Prior to the present experiment, the photoproduction of neutral kaons on a carbon target near the threshold energy was measured for the first time at the Laboratory of Nuclear Science (LNS) of Tohoku University [22]. Neutral kaons were detected via the $K_S^0 \rightarrow \pi^+\pi^-$ decay channel using the Neutral Kaon Spectrometer (NKS). The cross sections were compared with those for K^+ photoproduction [23] as a function of the incident photon energy. It was found that the cross sections for K^0 and K^+ production on ^{12}C are almost of the same magnitude. The momentum spectra of kaons were also compared with simple model calculations based on recent isobar models for elementary production processes. However, analysis of the elementary reaction was limited because of the uncertainty due to the complex many-body nature of the process on the carbon target.

As a next step, we carried out measurements of neutral kaons with the NKS using a liquid deuterium target and report the results in this article. In Sec. II, the experimental apparatus and methods are described. In Sec. III, event selection, derivation of the K^0 momentum distributions, estimation of the background, and detection efficiencies are discussed. Section IV presents results for momentum spectra for the deuteron target and their comparison with theoretical predictions. The conclusion is given in Sec. V.

II. EXPERIMENTAL APPARATUS

The K^0 meson was inclusively measured via the $\pi^+\pi^-$ decay channel using the NKS, which was constructed and installed in the second experimental hall equipped with the STB-Tagger system [24] at LNS. The NKS was originally used as the TAGX spectrometer at the electron synchrotron of the Institute of Nuclear Study, University of Tokyo (INS-ES) [25]. In this section, the apparatuses of the beam line and the detectors of the NKS are described.

A. Tagged-photon beams

Figure 1 shows the experimental setup. A 200-MeV electron beam from the linear accelerator was injected into the STretcher Booster (STB) ring, accelerated up to 1.2 GeV typically in 1.2 s, and then stored for 20 s in the ring. Bremsstrahlung photons were generated by inserting a radiator

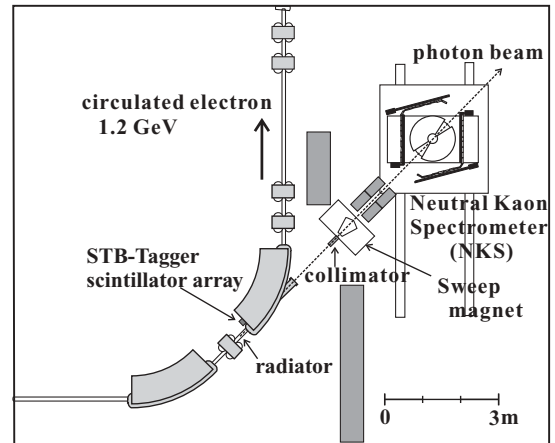


FIG. 1. Top view of the experimental setup in the second experimental hall at LNS. The electrons were accelerated up to 1.2 GeV in the accelerator ring. Bremsstrahlung photons were generated by inserting a radiator. The scattered electrons were detected by the STB-Tagger. A collimator and a sweep magnet were set on the photon beam line to remove the beam halo and the background from the e^+e^- pair creation.

made of a carbon fiber of $11\ \mu\text{m}$ ϕ at the entrance of one of the bending magnets. The generated photon energy was tagged by analyzing the momentum of a scattered electron with the bending magnet [24]. The tagging counter consisted of 50 plastic scintillators, the time resolution being evaluated to be 240 ps. The duty factor was about 64% with an 18-s beam every 25 s.

The tagged energy range was 0.8–1.1 GeV and the accuracy of the energy was estimated to be $\Delta E = \pm 10$ MeV (see Sec. II A 1). The total count rate of the counter array was 2 MHz on average.

As shown in Fig. 1, a sweep magnet of about 1.0 T and 0.5 m in length was located between an extraction window and the NKS to suppress the background of the e^+ and e^- created at the exit window of the photon beam. In addition, a 25-cm-long lead collimator with a 1.0-cm-diameter aperture was placed just upstream of the sweep magnet to remove the photon beam halo. Furthermore, two helium bags were installed in the space between the sweep magnet and the target. The windows of the bags along the beam line were made of Mylar film 10 μm in thickness. The size of the photon beam at the target was 3–5 mm (σ).

1. Energy calibration

Energy calibration of the STB-Tagger system was carried out prior to the series of K^0 photoproduction experiments with the NKS.

In the calibration experiment, the sweep magnet was used as a spectrometer for e^+e^- pairs generated in the $\gamma \rightarrow e^+e^-$ conversion process. A copper converter of 0.9 mm ϕ was installed upstream of the magnet. The e^+e^- pairs were detected by a drift chamber installed downstream of the magnet. The momenta of the e^+e^- pairs were analyzed using the magnetic field distribution calculated by the three-dimensional finite

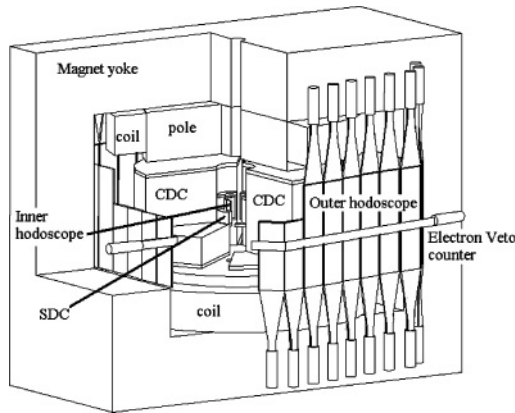


FIG. 2. Schematic drawing of the NKS. The drift chambers (CDC, SDC) were set among the poles.

element method program (TOSCA). Finally, the photon energy was derived by $E_\gamma = E_{e^+} + E_{e^-}$. The precision of the photon energy was determined to be ± 10 MeV considering the uncertainty of the magnetic field distribution.

B. NKS

Figure 2 shows a schematic drawing of the NKS and Fig. 3 shows the detector configuration. The spectrometer consisted of a 0.5-T dipole magnet 107 cm in diameter and with a 60-cm gap, with a pair of cylindrical drift chambers (CDC), a pair of straw drift chambers (SDC), inner and outer scintillator hodoscopes (IH, OH), and electron veto scintillation counters (EV).

IH surrounded the target 6 cm from the center. It was segmented into 12 pieces 12 cm in height and 0.5 cm in thickness, covering the angular range from ± 15 to $\pm 160^\circ$. The scintillation photons were guided from the bottom end of each scintillator to the outside of the magnet gap through bundles of optical fibers about 1.5 m long. The time resolution of IH was about 470 ps (σ).

SDC covered the angular range from ± 10 to $\pm 170^\circ$ and the radial range from 7.18 to 10.19 cm. SDC had four layers of sense wires made of gold plated tungsten of $20 \mu\text{m}$ ϕ with straw tubes made of aluminized Mylar film $180 \mu\text{m}$ thick.

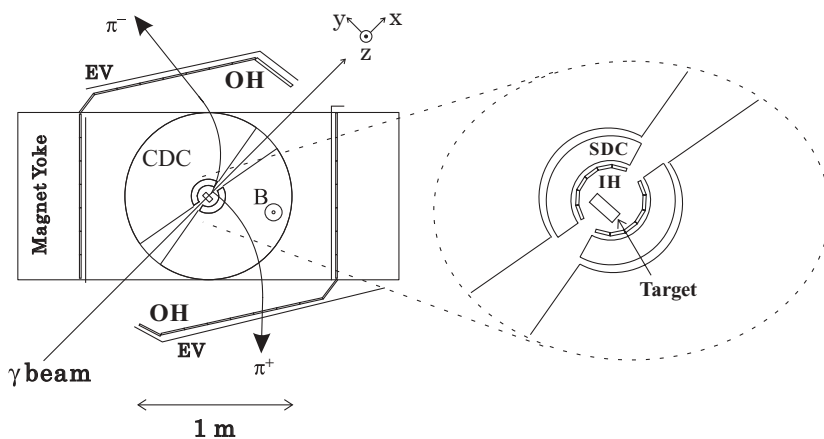


FIG. 3. Floor plan of the detector configuration and an example of two pion trajectories. The detectors were placed almost symmetrically along the beam line.

CDC covered the angular range from ± 15 to $\pm 165^\circ$ and the radial range from 13.8 to 48.6 cm. Field wires were arranged hexagonally around a sense wire. Because all the wires were vertical, the information of the track position was horizontal only. CDC had 12 layers grouped into four groups, each having 3 layers. In the present experiment, 9 of the 12 layers were used because the third layer of each group was not active. The CDC sense wires were made of gold-plated tungsten of $30 \mu\text{m}$ ϕ for the inner two layers and of stainless steel for the third layer. The field wires were made of molybdenum of $100 \mu\text{m}$ ϕ . The drift chamber gas was a mixture of argon (50%) and ethane (50%). High voltages were applied to the sense wires, typically +3000 V for CDC and +1900 V for SDC. The spatial resolutions were about $400 \mu\text{m}$ for CDC and $500 \mu\text{m}$ for SDC.

OH hodoscopes were installed outside the drift chambers. They were segmented into 34 pieces, the size of each counter being about 60 cm in height, 1.0 cm in thickness, and typically 15 cm in width. Some of the scintillators were placed inside the magnet gap as shown in Fig. 3, and the scintillation photons were guided outside the magnet through the bundle of optical fibers. All the OH had photomultiplier tubes (PMT) at both ends and provided information on the time-of-flight between IH and OH with a time resolution of 510 ps. The vertical position of charged particles hitting an OH was also given by the time difference of the signals from two PMTs. The vertical position resolution of OH was about 4 cm.

The geometrical acceptance of NKS was about π sr and the momentum threshold was 80 MeV/c. K^0 s were identified by the invariant mass of the $\pi^+\pi^-$ pair measured in coincidence with the left and right detector arms.

EV scintillators were installed on the midplane of the NKS and next to the OH array, as shown in Fig. 3, to reject e^+e^- pairs that were distributed in the midplane and causing large background trigger. They covered a vertical range ± 2.5 cm at the OH array and therefore the NKS geometrical acceptance was reduced by about 8%.

C. Liquid deuterium target

The liquid deuterium target was inserted through the central holes of the pole and the yoke of the NKS magnet from the top of the yoke. The cryostat had a cylindrical part of 1200 mm

long with a diameter of 100 mm for the insertion. The target cell was contained at the lower end of the cryostat. The two-stage Gifford-McMahon refrigerator (Sumitomo Heavy Industry RD208B) was attached at the top of the cryostat. An oxygen free copper rod with a diameter of 25 mm and a length of 942 mm connected the second stage and the condenser placed near the target cell. The deuterium gas was precooled at the first stage, liquified at the condenser, and then stored in the cell.

The target cell was cylindrical and placed with its axis parallel to the beam line. The length of the cylinder was 30 mm and the diameter was 50 mm. The cylindrical shell was made of aluminum 1 mm in thickness and its entrance and exit window were covered with polyimide (Ube UPILEX-S) films 75 μm in thickness. The vacuum chamber of the cryostat surrounding the target cell was made of carbon fiber reinforced plastic (CFRP) 1.5 mm in thickness. It also had an entrance window of 40 mm for the γ beam covered with a polyimide film 75 μm in thickness. The target cell was placed at 15 mm upstream from the center of the NKS. The thickness and the position of the target was optimized by a simple simulation for the K^0 yield.

The typical temperature of the liquid deuterium was 19 ± 1 K, the pressure 50 ± 2 kPa, and the density 0.17 g/cm^3 in the data taking period. The target system was remotely controlled and monitored with a LabView program running on a Linux-PC for easy and secure access via the network.

D. Data acquisition system

The data for the hodoscope and tagger counters were fed into the TDC and ADC modules of the TKO, which is a data acquisition system developed at KEK [26], then stored in a VME memory module (SMP), and read event by event by a Linux-PC through a VME-PCI interface module (Bit3-617). The signals of the drift chambers were preamplified and sent to the amplifier-discriminator cards about 7 m away from the chambers. The digitized data were transferred by 70-m twisted pair cables to the counting room and were recorded by the Lecroy 4290 TDC system. These data were also read by a Linux-PC through a CAMAC interface (TOYO CC7700).

A trigger signal was generated when more than two charged particles were detected in coincidence with the IH and OH in both the left and right arms and at least one hit in the tagger counters. As mentioned before, the EV was used as a veto in the trigger.

The data-acquisition efficiency was typically 90% with a trigger rate of 100 Hz.

III. ANALYSIS AND RESULTS

K^0 was identified and measured by $K^0 \rightarrow \pi^+\pi^-$ decay in the invariant mass of $\pi^+\pi^-$. $\pi^+(\pi^-)$ was identified from the momentum, charge, and velocity. The horizontal momenta of the charged particles were calculated from the curvature of the trajectories, and the vertical momentum information was extracted assuming that a vertical projection was a straight line between the spectrometer center and the OH. The particle

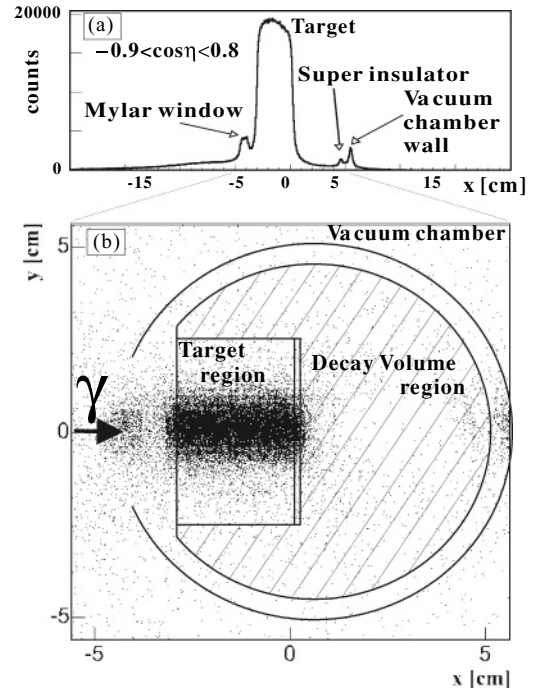


FIG. 4. (a) Vertex point distribution along the beam line for the deuterium target after applying a cut of the opening angle (η). (b) Scatter plot of the vertex point distribution around the target. The contribution from the walls of the vacuum chamber is also seen.

velocities were obtained from the flight length and the time-of-flight between the IH and the OH.

A. Event selections

e^+e^- pair production was the largest source of background, even using the EV veto in the trigger level. In the analysis, e^+e^- pairs generated upstream of the target were removed by rejecting upstream vertex points. Figure 4(a) shows a distribution of vertex points along the beam line axis. Because the acceptance for e^+e^- events generated near the target was much smaller than that for those generated in the upstream region, most of the e^+e^- events were removed. Furthermore, a cut for the opening angle (η), $-0.9 < \cos \eta < 0.8$, was applied to remove the e^+e^- pairs because the opening angle of e^+e^- was much smaller than that of $\pi^+\pi^-$ from K^0 decay.

Figure 5 shows a scatter plot of inversed velocities vs momenta of particles after applying the cut of the opening angle and selecting decay points near the target. The sign of the momentum represents the charge of the particle. The particles were identified by selecting the region-defined-lines in Fig. 5.

Figure 4(b) shows the vertex point distribution around the target for $\pi^+\pi^-$ events. The materials around the target are also indicated in the figure. The resolution of the x position of the vertex was about 1.3 mm.

Figure 6 shows the spectra of the $\pi^+\pi^-$ invariant mass for events with vertex points in the target (a) and out of the target (b). For events in the target region, K^0 events were hidden in the

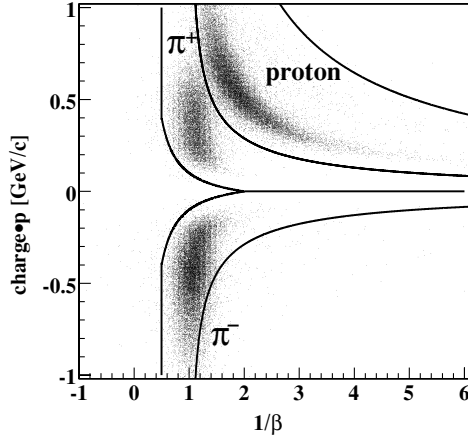


FIG. 5. Scatter plot of β^{-1} vs momentum. The sign of the momentum represents the charge of the particle. The opening angle cut, $-0.9 < \cos \eta < 0.8$, and the selection of the vertex points near the target are applied to remove e^- and e^+ . The solid lines represent the selected region as protons or pions.

invariant mass spectrum because the spectrum is dominated by processes not involving strangeness, such as production of ρ , nucleon resonances, and others. These particles immediately decay by the strong interaction. In contrast, for events whose vertex points were reconstructed outside of the target, a peak of K^0 is clearly seen because a considerable fraction of K_S^0 decays outside of the target because of the relatively long lifetime of $c\tau \sim 2.68$ cm. Thus, we defined the decay volume as the hatched area shown in Fig. 4(b) to select K_S^0 .

$$\frac{d^2\sigma}{d\Omega dp} = \frac{N_{\text{yield}}(p, \cos \theta)}{N'_\gamma \cdot N_{\text{target}} \cdot \epsilon_{\text{acpt}}(p, \cos \theta) \cdot \epsilon_{\text{DAQ}} \cdot \epsilon_{\text{track}} \cdot \epsilon_{\text{gate}} \cdot 2\pi \Delta(\cos \theta) \Delta p},$$

where N_{yield} , N'_γ , and N_{target} are the number of selected K^0 events, the number of photons bombarding the target, and the number of target neutrons, respectively. p and $\cos \theta$ are the K^0 momentum and the emitted angle to the photon beam line in the laboratory frame, $\epsilon_{\text{acpt}}(p, \cos \theta)$ is the acceptance of the NKS for K^0 detection, ϵ_{DAQ} is the data taking efficiency, ϵ_{track} is the tracking analysis efficiency, and ϵ_{gate} is the efficiency due to the gating K^0 mass spectrum.

The acceptance [$\epsilon_{\text{acpt}}(p, \cos \theta)$] shown in Fig. 8(a) was evaluated by analyzing the simulated data generated by the Geant4 program taking into account the geometry of the NKS, the trigger condition, and the detector resolutions. As demonstrated in Fig. 8, the acceptance reached a broad maximum in the forward region and momentum region of about 0.3 GeV/c.

In the following, the data in the selected region, $0.1 < p_{K^0, \text{Lab}} < 0.75$ GeV and $0.9 < \cos \theta_{K^0, \text{Lab}} < 1.0$ as indicated in Fig. 8(b), are analyzed.

Figure 9 shows the K^0 momentum distribution in the selected regions for the two beam energies. The

B. Background estimation

Even after the background was suppressed as described in the previous section, a background contribution still existed in the $\pi^+\pi^-$ invariant mass spectrum as shown in Fig. 6. The possible origins of the background were considered to come from

- (i) the imperfect rejection of nonstrangeness events such as ρ production due to the finite resolution of the vertex points and
- (ii) the combinatorial background of $\pi^+\pi^-$, such as π^+ from K_S^0 and π^- from Λ .

The shape of background (1) was assumed to be the same as that of events whose vertex points were reconstructed in the target region because those events were considered to have almost the same kinematics. On the other hand, the shape of background (2) was evaluated by Geant4 simulation.

Figure 7 shows $\pi^+\pi^-$ invariant mass spectra fitted assuming a Gaussian shape for the K_S^0 peak and the predetermined shapes for the two backgrounds. The fitting errors of the background spectra were typically 4% for background (1) and 8% for background (2). The widths of the K_S^0 peak around 0.5 GeV/c² were 16.2 ± 0.8 MeV/c² for the lower beam energy region ($0.9 \leq E_\gamma < 1.0$ GeV) and 13.0 ± 1.4 MeV/c² for the higher beam energy region ($1.0 \leq E_\gamma < 1.1$ GeV). In further analysis, the mass gate between 0.46 and 0.54 GeV/c² was applied to select K^0 events.

C. K^0 momentum spectra

The differential cross section of neutral kaons is given by

contributions of the backgrounds described in Sec. III B are also plotted.

The number of tagged photons irradiating the target (N'_γ) was obtained to be 1.03×10^{10} for $0.8 \leq E_\gamma < 0.9$ GeV, 1.16×10^{10} for $0.9 \leq E_\gamma < 1.0$ GeV, and 1.03×10^{10} for $1.0 \leq E_\gamma \leq 1.1$ GeV from the scaler counts of tagging counters after correcting for the tagging efficiency and the analysis efficiency of the tagging counter array. The tagging efficiency was estimated using the data by a lead glass Čerenkov counter (LG) positioned 260 cm downstream from the experimental target position on the beam line. The efficiency of the tagger counter was totally derived to be 71%.

The density of the deuterium target (N_{target}) was evaluated to be 0.173 g/cm³ from its temperature and vapor pressure. The expansion of the target cell due to the pressure of liquid deuterium was estimated by a finite element method and was found to be 1.58 mm for both sides. Therefore, the typical area density was obtained to be 0.172×10^{24} (cm⁻²).

The tracking efficiency (ϵ_{track}) was estimated to be typically 81.4% using π single-track events. It has a small dependence

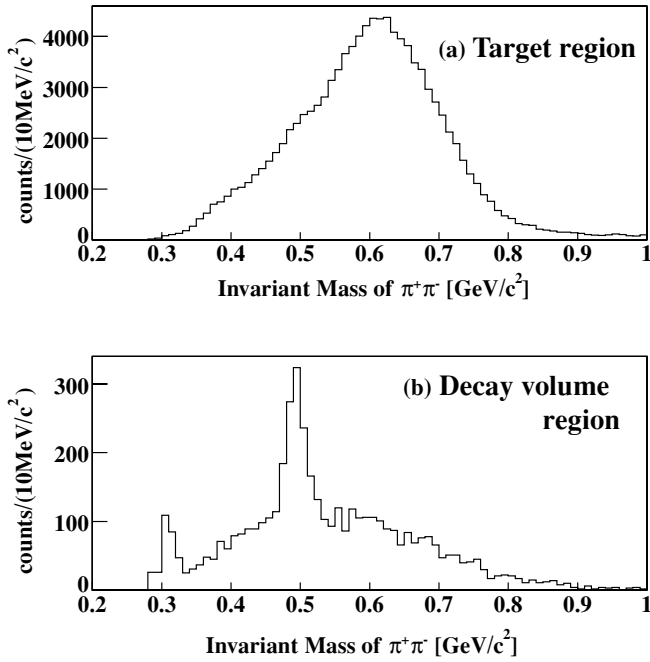


FIG. 6. Invariant mass spectrum of $\pi^+\pi^-$ (a) in the target region and (b) in the decay volume. The peak at 0.3 GeV/c^2 is caused by low momentum e^+e^- events identified as $\pi^+\pi^-$.

on the emission angle of the track due to a high counting rate at the forward angles. The efficiency decreases by 5% at most in the very forward angle and this dependence was taken into account in the analysis.

Table I summarizes the efficiencies and their statistic and systematic errors.

The total systematic error was estimated to be about $\pm 10\%$ by the square root of the sum of the squares of the listed efficiencies.

Taking into account all of these efficiencies, K^0 momentum spectra were derived in the two photon-energy regions as shown in Fig. 10. The contributions of the background were subtracted in the cross sections.

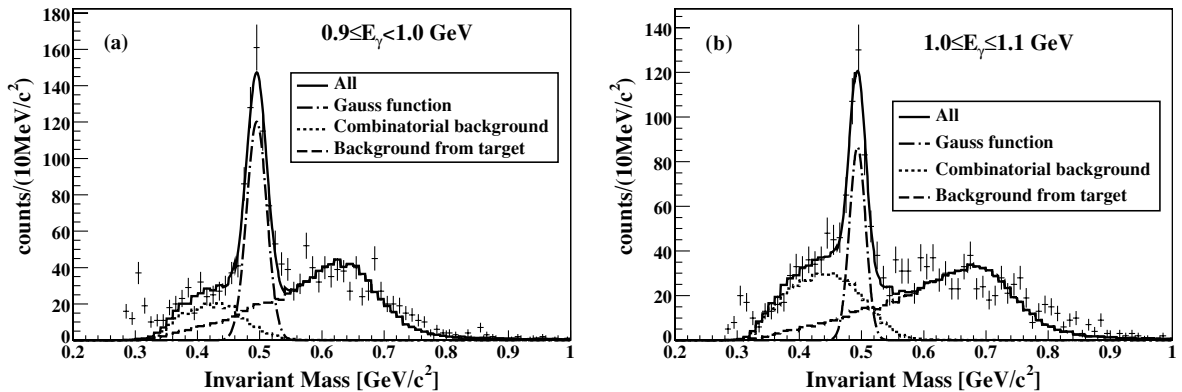


FIG. 7. Fitting results for $\pi^+\pi^-$ invariant mass spectra in the photon energy ranges (a) from 0.9 to 1.0 GeV and (b) from 1.0 to 1.1 GeV . The contribution around 0.4 GeV/c^2 comes from the combinatorial background and that around 0.6 GeV/c^2 comes from other processes produced in the target region.

TABLE I. Summary of efficiencies and numbers are listed. Some of them are not constant and are listed for typical values. Systematic errors are estimated from the fluctuations among the experimental periods or the fluctuations of photon intensity.

	Value	Statistical error	Systematic error
ϵ_{gate}	95.4%	$<0.1\%$	$\pm 4\%$
$N'_\gamma(\text{all})$	3.22×10^{10}	$\pm 1.0\%$	$\pm 4.7\%$
N_{target}	0.172 (barn^{-1})	$<0.1\%$	$\pm 0.6\%$
ϵ_{DAQ}	89.1%	$<0.1\%$	$\pm 1.0\%$
ϵ_{track}	81.4%	$<0.1\%$	$\pm 8.1\%$

IV. DISCUSSIONS

A. Theoretical calculations

The inclusive cross sections for the $d(\gamma, K^0)YN'$ process, where $Y = \Lambda, \Sigma^0$, and Σ^+ , and N' is the corresponding nucleon, were compared with a simple spectator model calculation in the plane wave impulse approximation with a spectator nucleon (N') [27]. The energy of the target nucleon (N) is given by $E_N = m_d - E_{N'} = E_{K^0} + E_\Lambda - E_\gamma$ for the off-shell approximation, to satisfy energy conservation in the elementary process, and by $E_N = \sqrt{m_N^2 + \vec{p}_N^2}$ for the on-shell approximation. The effective mass of the target nucleon is determined as $\tilde{m}_N = \sqrt{p^\mu p_\mu}$ and $\vec{p}_N = -\vec{p}_{N'}$. The momentum distribution of the target nucleon is described by the nonrelativistic Bonn deuteron wave function OBEPQ (one boson exchange potential in q space) [28].

Differences in results caused by employing the on- and off-shell approximations and other deuteron wave functions were found to be small or negligible in the kinematical region studied in the present experiment [27]. In the following analysis, we use the off-shell approximation. Moreover, we assume that the contribution of the final-state interaction to the inclusive kaon momentum distribution [29] is small in our kinematics and therefore that our model is sufficient for a description of the process (at least in the quasifree region).

The largest uncertainty in the calculated K^0 momentum distribution came from the choice of the elementary

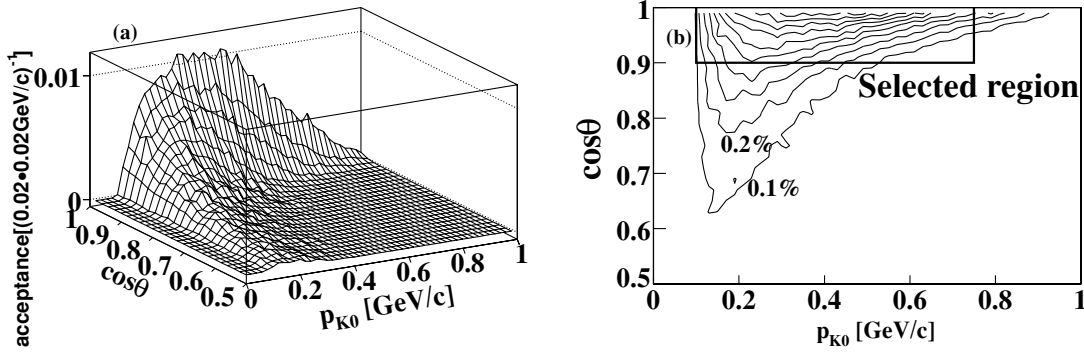


FIG. 8. Acceptance map of the NKS evaluated by simulation shown as a function of the K^0 momentum and the cosine of the emitted angle with the photon beam line in the laboratory frame. The solid box in (b) shows the accepted region, which has an efficiency larger than 0.1%.

amplitude [27]. We used three different models for the elementary amplitude, two isobar models, Kaon-MAID [20] and Saclay-Lyon A (SLA) [19], and a simple phenomenological prescription, to analyze the angular dependence of the elementary cross section in the center-of-mass frame (c.m.).

In the isobar models, the cross sections for channels that include K^0 in the final state were calculated assuming isospin symmetry for the strong coupling constants and appropriately adopting electromagnetic coupling constants for the neutral mode by replacing those for the charged mode [20]. For the t -channel meson resonances, the ratio of the coupling constants for neutral and charged modes is related to the ratio of the decay widths, which is well known for $K^*(892)$ but unknown for the K_1 resonance [30]. The ratio for the latter, $r_{K_1K\gamma}$, is therefore treated as a free parameter and has to be determined from data. In the case of the Kaon-MAID model, the cross section of the $n(\gamma, K^0)\Lambda$ reaction can be predicted because the parameter was determined by simultaneous fitting of the $K^0\Sigma^+$ channel.

On the other hand, in the SLA model, the parameters were adjusted only from $K^+\Lambda$ production data and the model cannot predict the $K^0\Sigma$ channel contributions. The electromagnetic coupling constants of the only s -channel

resonance in SLA, $N^*(1720)$, were therefore changed in the $K^0\Lambda$ process using relations between the coupling constants and the helicity amplitudes, which can be taken from the Particle Data Group tables [30], as it is done in the Kaon-MAID model [20]. The values for $N^*(1720)$ used in our calculations are $g_{N^*n\gamma}^1/g_{N^*p\gamma}^1 = -2.24$ and $g_{N^*n\gamma}^2/g_{N^*p\gamma}^2 = 0.42$ [20]. In the t channel, if the value $r_{K_1K\gamma} = -0.45$ determined in Kaon-MAID [31] is used in SLA, it gives a cross section several times larger than that of Kaon-MAID. Therefore, when $K^0\Lambda$ production is calculated with SLA, $r_{K_1K\gamma}$ is assumed as a free parameter.

To show the angular dependence of the elementary cross section preferred by the data, a simple phenomenological parametrization in c.m., named PH, was also used:

$$\frac{d\sigma}{d\Omega} = \sqrt{(s - s_0)}(1 + e_0(s - s_0))(a_0 P_0(x) + a_1 P_1(x) + a_2 P_2(x)). \quad (1)$$

Here $P_l(x)$ are Legendre polynomials, $x = \cos(\theta_K^{c.m.})$, s is the square of the photon-nucleon c.m. energy, and $s_0 = 2.603 \text{ GeV}^2$, the $K^0\Lambda$ threshold. Because the invariant cross section is inversely proportional to the final c.m. momentum, which behaves as $\sqrt{(s - s_0)}$ near the threshold, the

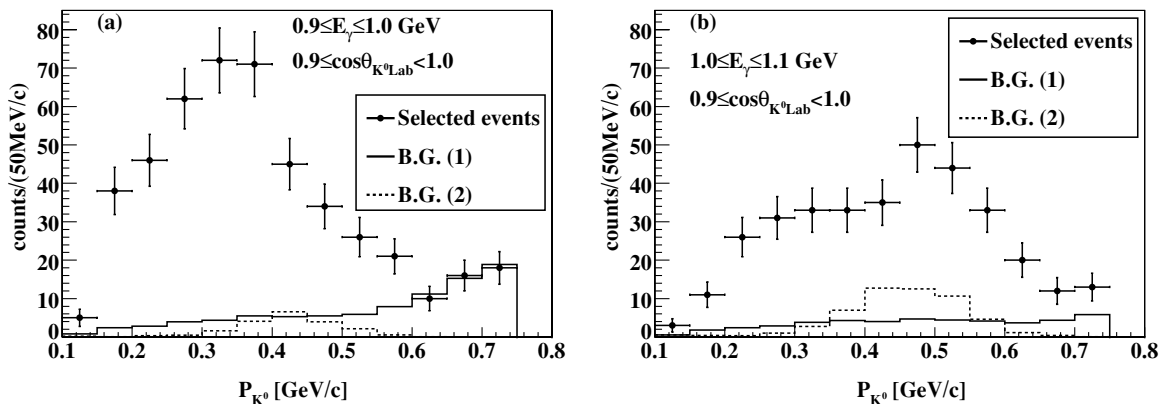


FIG. 9. Momentum distributions for K^0 in the selected region of the NKS acceptance for events in the decay volume (closed circles), the background from the target region [solid line, B.G. (1)], and the combinatorial background [dashed line, B.G. (2)]. The error bars show the statistic errors.

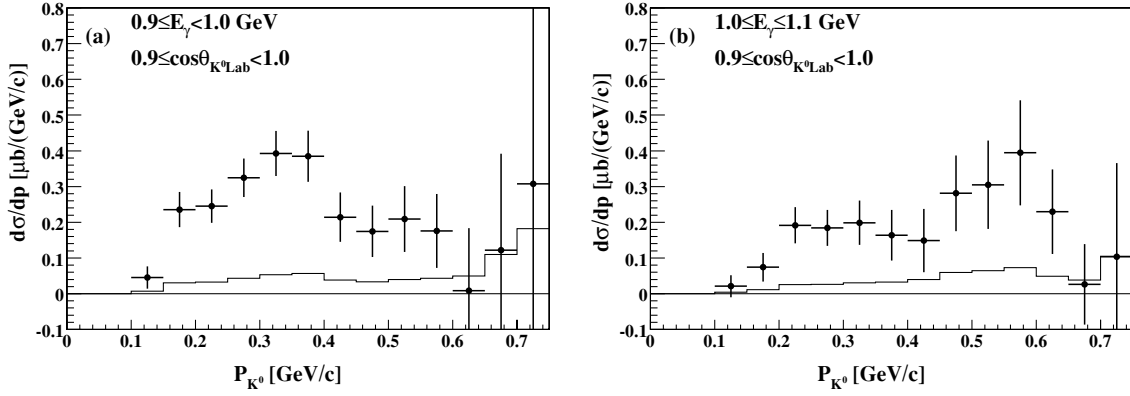


FIG. 10. Inclusive momentum spectra for K^0 photoproduction in the selected region of the NKS acceptance. The photon energies and kaon angles are displayed in the figure. The error bars show the statistical errors. The systematic error is represented by solid histograms on the baseline.

energy-dependent factor of this form is included in Eq. (1) to regularize the invariant cross section.

B. Comparison of data with calculations

The measured inclusive spectra of the $K^0 Y$ channels are shown in Fig. 11 together with theoretical curves. Contributions of the Σ photoproduction processes calculated with Kaon-MAID are also shown. These contributions are estimated to be at the very most 5% in the lower photon-energy region but up to 60% at the K^0 momentum of 0.3 GeV/c in the higher photon-energy region. Therefore, the $r_{K_1 K \gamma}$ parameter of SLA was deduced from the data only in the lower photon-energy region where the contribution of the Σ channels was sufficiently small. The enhancement of the data points around 0.3 GeV/c seen in the higher photon-energy region can be attributed to Σ photoproduction, which, however, cannot be evaluated with SLA.

In both energy regions, it is found that Kaon-MAID gives cross sections larger than the present measured spectra and the shape of the calculated momentum spectra are considerably different from that of the data.

The theoretical spectrum with SLA was fitted with the $r_{K_1 K \gamma}$ parameter in the lower photon-energy region. The magnitude and shape of the momentum spectrum are reproduced well for $r_{K_1 K \gamma} = -2.087$. Note that this value is related to the ratio of the decay width of the K_1 meson, $\Gamma_{K_1^0 \rightarrow K^0 \gamma} / \Gamma_{K_1^+ \rightarrow K^+ \gamma} = r_{K_1 K \gamma}^2 = 4.36$. The magnitude of the cross section in the higher energy region is reproduced better by SLA than by Kaon-MAID.

The difference of the shape of the momentum spectra in the laboratory system between Kaon-MAID and SLA in the lower photon-energy region is caused by the different angular distribution of the elementary cross sections in the c.m. system, as shown in Fig. 12. The data, therefore, suggest that an enhancement of the elementary cross section in the backward hemisphere is crucial to explain the K^0 momentum spectrum shape. On the other hand, in the higher photon-energy region,

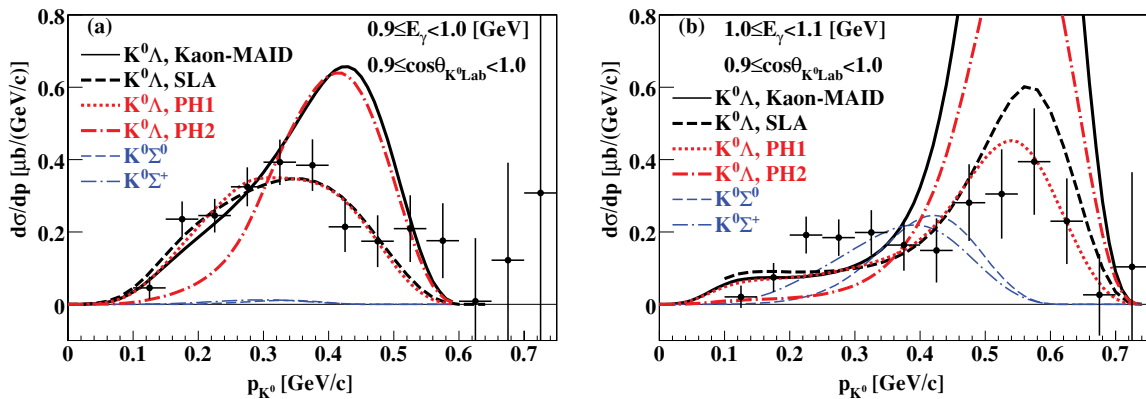


FIG. 11. (Color online) Inclusive momentum spectra for K^0 photoproduction in the effective regions in comparison with calculations for the $K^0 \Lambda$ channel using elementary amplitudes of Kaon-MAID [20] (black, solid line), SLA [19] with $r_{K_1 K \gamma} = -2.09$ (black, dotted line), PH1 (red, dashed line), and PH2 (red, dash-dotted line) models. The contribution of the $K \Sigma$ channels calculated by using Kaon-MAID are also shown (blue, slim dashed and slim dash-dotted line). The photon energies and kaon angles are displayed in the figure. The error bars show statistical errors. The systematic error is not represented.

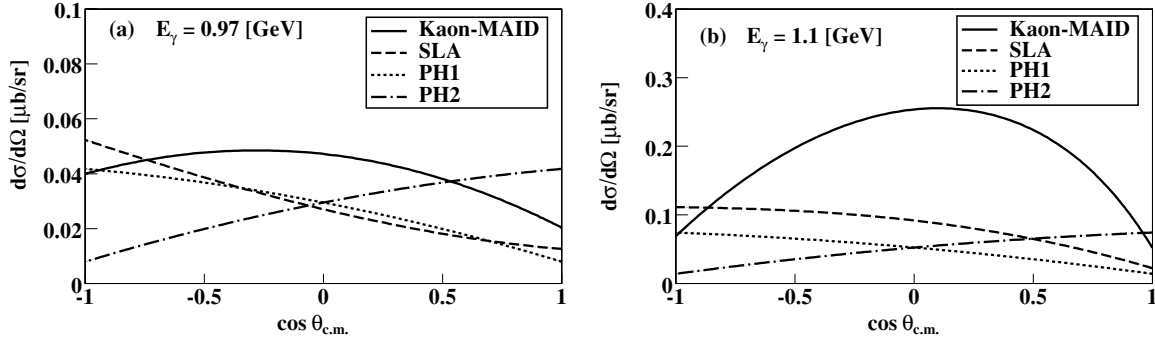


FIG. 12. Angular distributions of the elementary cross section of $K^0\Lambda$ production in the c.m. system for (a) $E_\gamma = 0.97$ GeV and (b) $E_\gamma = 1.1$ GeV. The Kaon-MAID [20] (solid line), SLA [19] with $r_{K_1K\gamma} = -2.09$ (dotted line), PH1 (dashed line), and PH2 (dash-dotted line) models are shown.

the difference of the momentum spectra is due not only to the angular distribution but also to the magnitude of the cross section, as seen in Fig. 12(b).

To confirm these points, the spectrum in the lower photon-energy region were fitted by Eq. (1), in which the angular distribution is given by Legendre polynomials up to second order. The best-fit parameters (PH1) were obtained: $a_0 = 0.0884$, $a_1 = -0.0535$, $a_2 = -0.0098$, and $e_0 = -0.132$ with $\chi^2/n.d.f. = 1.19$. The phenomenological parametrization with the opposite sign of a_1 (PH2), giving the inverse angular distribution to that of PH1, is also shown in Figs. 11 and 12. In Fig. 11, it is shown that PH1, having a backward angular distribution in c.m. similar to that of SLA, gives a very good agreement with the present data in both photon-energy regions. On the other hand, PH2, giving a momentum spectrum similar to that of Kaon-MAID and a forward peaked angular distribution in contrast to PH1, clearly contradicts the present result. Thus, a comparison of the data and predictions of models favors an angular distribution of the $n(\gamma, K^0)\Lambda$ reaction in the c.m. system that is peaked at backward angles.

In Fig. 13, the photon energy dependence of the total cross section for $K^0\Lambda$ photoproduction is given for SLA with $r_{K_1K\gamma} = -2.087$, Kaon-MAID, and the PH1 and PH2 parametrizations. The K^0 total cross sections are not obtained in the present experiment because of the limited kinematical

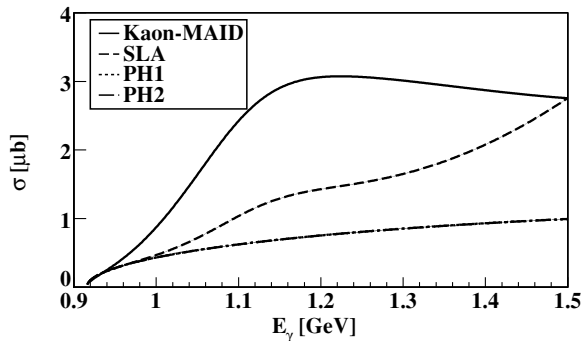


FIG. 13. Calculated photon-energy dependence of the total cross section of $K^0\Lambda$ production for the Kaon-MAID [20] (solid line), SLA [19] with $r_{K_1K\gamma} = -2.09$ (dotted line), PH1 (dashed line), and PH2 (dash-dotted line) models are shown.

acceptance for K^0 . Kaon-MAID predicts a very sharp rise in the photon-energy dependence of the K^0 total cross section near the threshold ($E_\gamma < 1.2$ GeV), while SLA, as well as PH1 and PH2, gives a flatter energy dependence and much smaller cross section in the threshold region.

V. SUMMARY

K^0 photoproduction on a deuterium target was studied in the threshold region for the first time. The experiment was conducted at LNS of Tohoku University following the measurement of quasifree photoproduction of K^0 on a carbon target.

Inclusive momentum distributions were obtained and compared with theoretical calculations. The calculations were performed in the plane wave impulse approximation using a realistic Bonn wave function OBEPQ for a deuteron, first with the recent isobar models, Kaon-MAID and Saclay-Lyon A, and second with simple phenomenological parametrization. Based on the comparison, the angular distributions of the elementary cross sections were examined.

The best agreement with the data was achieved with the SLA model, in which the ratio of the neutral-to-charged electromagnetic coupling constants for the K_1 meson was obtained to be $r_{K_1K\gamma} = -2.09$ by fitting data in the photon energy region, $E_\gamma = 0.9\text{--}1.0$ GeV, and with phenomenological parametrization fitted in the photon energy region, $E_\gamma = 0.9\text{--}1.0$ GeV. Both models show enhancement of the c.m. cross section in the backward hemisphere. The present result, therefore, sets constraints on models for the photo- and electroproduction of kaons in the threshold region. This study shows that the $n(\gamma, K^0)\Lambda$ reaction with its unique feature is important for the investigation of the strangeness photoproduction.

ACKNOWLEDGMENTS

This work is supported by Grants-In-Aid for Scientific Research from The Ministry of Education of Japan, Nos. 09304028, 12002001, and 14740150, and by the Grant Agency of the Czech Republic under Grant 202/05/2142.

- [1] R. L. Anderson, E. Gabathuler, D. Jones, B. D. McDaniel, and A. J. Sadoff, *Phys. Rev. Lett.* **9**, 131 (1968).
- [2] C. W. Peck, *Phys. Rev.* **135**, B830 (1964).
- [3] D. E. Groom, *Phys. Rev.* **159**, 1213 (1967).
- [4] A. Bleckmann *et al.*, *Z. Phys.* **239**, 1 (1970).
- [5] T. Fujii *et al.*, *Phys. Rev. D* **2**, 439 (1970).
- [6] P. Feller, D. Menze, U. Opara, W. Schulz, and W. J. Schwillie, *Nucl. Phys.* **B39**, 413 (1972).
- [7] R. Erbe *et al.*, *Phys. Rev.* **188**, 2060 (1969).
- [8] K. H. Althoff *et al.*, *Nucl. Phys.* **B137**, 269 (1978).
- [9] H. Thom, *Phys. Rev.* **151**, 1322 (1966).
- [10] K. H. Glander *et al.* (SAPHIR Collaboration), *Eur. Phys. J. A* **19**, 251 (2004).
- [11] R. Bradford *et al.* (CLAS Collaboration), *Phys. Rev. C* **73**, 035202 (2006).
- [12] M. Sumihama *et al.* (LEPS Collaboration), *Phys. Rev. C* **73**, 035214 (2006).
- [13] R. Bradford *et al.* (CLAS Collaboration), *Phys. Rev. C* **75**, 035205 (2007).
- [14] R. A. Adelseck and B. Saghai, *Phys. Rev. C* **42**, 108 (1990).
- [15] R. A. Williams, C. R. Ji, and S. R. Cotanch, *Phys. Rev.* **46**, 1617 (1992).
- [16] J. C. David, C. Fayard, G. H. Lamot, and B. Saghai, *Phys. Rev. C* **53**, 2613 (1996).
- [17] C. Bennhold and L. E. Wright, *Phys. Rev. C* **39**, 927 (1989).
- [18] S. Janssen, J. Ryckebusch, D. Debruyne, and T. Van Cauteren, *Phys. Rev. C* **65**, 015201 (2001).
- [19] T. Mizutani, C. Fayard, G. H. Lamot, and B. Saghai, *Phys. Rev. C* **58**, 75 (1998).
- [20] F. X. Lee, T. Mart, C. Bennhold, and L. E. Wright, *Nucl. Phys.* **A695**, 237 (2001).
- [21] X. D. Li, L. E. Wright, and C. Bennhold, *Phys. Rev. C* **45**, 2011 (1992).
- [22] T. Watanabe *et al.*, *Phys. Lett.* **B651**, 269 (2007).
- [23] H. Yamazaki *et al.*, *Phys. Rev. C* **52**, R1157 (1995).
- [24] H. Yamazaki, *Nucl. Instrum. Methods* **536**, 70 (2005).
- [25] K. Maruyama *et al.* (TAGX Collaboration), *Nucl. Instrum. Methods A* **376**, 335 (1996).
- [26] T. K. Ohska *et al.*, KEK Report No. 85 10 (1985, unpublished); *IEEE Trans. Nucl. Sci.* **33**, 98 (1986).
- [27] P. Bydzovsky, M. Sotona, O. Hashimoto, and T. Takahashi (2004), arXiv:nucl-th/0412035.
- [28] R. Machleidt, K. Holinde, and C. Elster, *Phys. Rep.* **149**, 1 (1987).
- [29] A. Salam, K. Miyagawa, T. Mart, C. Bennhold, and W. Glöckle, *Phys. Rev. C* **74**, 044004 (2006).
- [30] W. M. Yao *et al.* (Particle Data Group Collaboration), *J. Phys. G* **33**, 1 (2006).
- [31] This value of $r_{K_1 K \gamma}$, which differs from that quoted in Ref. [20], has been used in a newer version of the Kaon-MAID model.